Simulation of the Air-Oil Mixture Flow in the Scavenge Pipe of an Aero Engine using Generalized Interphase Momentum Exchange Models

STRATIS KANARACHOS*, MICHAEL FLOUROS**
*Mechanical Engineering Department
Frederick University
7 Y. Frederickou St., Lefkosia 1036,
CYPRUS
eng.ks@frederick.ac.cy http://www.frederick.ac.cy

** Air and Oil Systems Group
MTU Aero Engines
Dachauer Strasse 665, Munich 80995,
GERMANY
michael.flouros@mtu.de http://www.mtu.de

Abstract: - Understanding the flow in aero-engine lubrication systems forms an essential part of future designs for aero-engines. This especially applies to scavenge pipes which contain a complex two-phase flow formed by the interaction of sealing airflow and lubrication oil. In the last decade, two phase flows in pipes are increasingly modeled and simulated with 3D Computational Fluid Dynamics (CFD) codes. One of the major challenges is to approximate the different flow morphologies developed (bubbly, stratified, annular, slug, e.t.c.) using a unified CFD model without increasing prohibitively the computational cost. This paper presents a methodology implementing empirically derived generalized interphase momentum exchange models for modeling and simulation of the two phase flow of air and oil in the scavenge pipe of an aero-engine. The advantage of the proposed approach is the simplicity of the computational model which depends mainly on the assumed bubble diameter. Simulation results are presented and discussed for an experimental study performed at MTU Aero Engines facilities. This work is part of the European Union funded research program ELUBSYS (Engine LUBrication System TechnologieS) within the 7th EU Frame Program for Aeronautics and Transport.

Key-Words: - Two phase flow; interphase momentum exchange model; aero-engine; scavenge pipe

1 Introduction

A scavenge pipe in the lubrication system of an aero engine is responsible for transporting the lubrication oil from the bearing chamber to the oil tank. Its purpose is to prevent oil storage in the chamber and to remove the generated heat to an outside cooling source. The vent pipe in the lubrication system is responsible for transporting the sealing air from the bearing chamber to the air-oil separator. Its purpose is to prevent high pressure development in the bearing chamber which may lead to pressure reversal with respect to the outside environment. A new lubrication system technology developed by MTU Aero Engines opens the way to the design of vent-less bearing chambers. With this technology the air-oil mixture in the bearing chamber has to be transported entirely by the scavenge pipe. It is necessary therefore to study the air-oil mixture flow to mitigate high pressure drops and/or hot spot areas. The former may lead to oil leakage and fire, while the latter to oil coking and deposit formation.

In the last decade, several attempts have been made to simulate two phase flows within pipes using 3D CFD codes. Significant progress has been achieved in the nuclear and chemical industry which has led to the validation of the computational tools used. However, the work has concentrated mainly on straight –horizontal or vertical– segments of pipes. Furthermore, in most cases only one flow pattern – the bubbly or slug flow- was present.

More specific, Ref. [1] presented multiphase flow models for the description of mono- and polydisperse bubbly flows in vertical pipes. They have employed the Eulerian framework of multiphase flow modelling in ANSYS CFX. The

models were taking into account interphase momentum transfer due to governing drag and non-drag forces. Furthermore, in the case of poly-disperse air–water bubbly flow the bubble size distribution, bubble break-up and coalescence processes as well as different gas velocities in dependency on the bubble diameter were taken into account with the inhomogeneous MUSIG model. Weaknesses in the characterization of bubble coalescence and bubble fragmentation have been identified. For investigation of flow solver convergence the gas holdup and the global mass balances for both phases in the vertical pipe were defined as monitored target variables. Reliable converged solutions could be obtained for a satisfied convergence criterion based on the maximum residuals of 10^{-5} and for a physical time scale of the fully implicit steady-state solution method of $t = 5{\cdot}10{-}3$ *s*. Both multiphase flow models for mono- and polydisperse bubbly flows have thoroughly been validated and compared to experiments of MT-Loop and TOPFLOW test facilities.

In Ref. [2] the authors have modelled the internal phase distribution of co-current, air-water bubbly flow in a horizontal pipeline using the volume averaged multiphase flow equations. The predicted gas volume fraction and the mean liquid velocity were compared with experimental data. A pseudo time step 0.005 s was used. Under-relaxation factors between 0.6 and 0.7 were adopted for all flow quantities. Pressure was never under-relaxed, as required by the SIMPLEC algorithm. The hybrid-upwind discretization scheme was used for the convective terms. At the pipe inlet, uniform gas and liquid velocities and average volume fractions have been specified. At the pipe outlet, a relative average static pressure of zero was specified. For initiating the numerical solution, average volume fraction and parabolic liquid velocity profile were specified. Good quantitative agreement with the experimental data was obtained.

In Ref. [3] CFD post-test simulations of horizontal stratified two phase flows were performed using the code ANSYS CFX. The Euler–Euler two fluid model with the free surface option was applied. The fluid-dependent shear stress transport (SST) turbulence models were selected for each phase. Damping of turbulent diffusion at the interface was not considered. The level at the inlet was varied according to the time history of the liquid level measured in the high-speed camera frames. The outlet boundary condition has been applied to the cross section at the other end of the horizontal channel and was pressure controlled. The outer walls of the channel were set as hydraulically smooth walls with a non-slip boundary condition applied to both gaseous and liquid phases. A second-order implicit scheme was used to approximate the transient terms. The time step size was constant with 10^{-3} *s*. A convergence in terms of the RMS values of the residuals to be less than 10−4 could be assured most of the time. Due to the geometrical scale of the horizontal channel it was not possible to resolve the spatial structure of the free surface into the micro-scale with the CFD model. Transitions from stratified to elongated bubble flow and from wavy to slug flow were observed at higher liquid superficial velocities than in the literature. This was attributed to the shorter channel length and would indicate that the flow regime is not fully established at the end of the test-section. The qualitative agreement between calculation and experiment was encouraging and showed that CFD can be a useful tool in studying horizontal two-phase stratified flow.

Ref [4] has presented a study regarding wavy stratified flows that turn into slug flows. The authors have used ANSYS CFX for the CFD calculations. An Algebraic Interfacial Area Density (AIAD) model on the basis of the mixture model was introduced. The AIAD model applies three different drag coefficients; for bubbles, for droplets and for free surface. Non-drag forces were neglected. The interfacial area density depends on the morphology of the phases. The model can distinguish between bubbles, droplets and the free surface using the local liquid phase volume fraction value. The switching from one correlation to another was implemented using an exponential blending function. A turbulence damping procedure has been employed at the interfacial area providing a solid wall-like damping of turbulence in both gas and liquid phases. The behavior of slug generation and propagation was qualitatively reproduced by the simulation, while local deviations required a continuation of the work.

In this paper, for the first time, simulation of the air-oil mixture flow in the scavenge pipe of an aero engine will be presented and compared with the experiment. It is a continuation of the work presented in Ref [5]. The pipework has an approximate length of 4.5 *m* and is a combination of straight, vertical and inclined segments with bends, expansion & contraction singularities. The major challenge was to approximate the different flow patterns (bubbly, annular, stratified, slug) developed at different pipework locations using a unified CFD model. In this context, a global model has been developed by applying generalized interphase momentum exchange closure models. The rest of

the paper is organized as follows. In Section 2 the mathematical model will be presented while an analytic description of the computational model will be given in Section 3. In Section 4 numerical results and comparisons with the experiment will be shown and discussed. Final conclusions and future work will be given in Section 5.

2 Mathematical model

2.1 Eulerian two phase flow

In this study the Euler-Euler formulation for multiphase flows has been employed. The phases are assumed to be interpenetrating continua. A complete set of phase averaged Navier–Stokes equations has to be solved for each phase. Following the methodology described in Ref. [6] no detailed accounting of the interphase boundary conditions is required.

The continuity equation for each phase is written as:

$$\frac{\partial}{\partial t}(r_a \cdot \rho_a) + \nabla(r_a \cdot \rho_a \cdot U_a) = S_{MSa} + \Gamma_{\alpha\beta} \quad (1)$$

where SMSa describes mass sources and Γαβ is the mass flow rate per unit volume from phase β to phase α. The latter term only occurs if interphase mass transfer takes place.

Coupling between the momentum equations of the phases is achieved by implementing interphase momentum exchange terms into the respective phase's momentum balance equations. The momentum equation for each phase is:

$$\begin{aligned}\frac{\partial}{\partial t}(r_a \cdot \rho_a \cdot U_a) + \nabla[r_a \cdot (\rho_a \cdot U_a \times U_a)] = \\ - r_a \cdot \nabla P_a + \nabla\left[r_a \cdot \mu_a \cdot \left(\nabla U_a + (\nabla U_a)^T\right)\right] + \\ \sum_{\beta=1}^{N_p}\left(\Gamma^{+}_{\alpha\beta} \cdot U_\beta - \Gamma^{+}_{\beta\alpha} \cdot U_a\right) + S_{Ma} + M_{a\beta}\end{aligned} \quad (2)$$

where S_{Ma} describes momentum sources due to external body forces as gravitational force and user defined momentum sources, Maβ describes the interfacial momentum exchange term and $\Gamma^{+}_{\alpha\beta} \cdot U_\beta - \Gamma^{+}_{\beta\alpha} \cdot U_a$ represents momentum transfer induces by interphase mass transfer. In this work, only the hydrodynamics of the two phases is considered. Mass transfer between the phases or chemical reaction is neglected. Therefore, the above equations simplify to:

$$\begin{aligned}\frac{\partial}{\partial t}(r_a \cdot \rho_a) + \nabla(r_a \cdot \rho_a \cdot U_a) = 0 \\ \frac{\partial}{\partial t}(r_a \cdot \rho_a \cdot U_a) + \nabla[r_a \cdot (\rho_a \cdot U_a \times U_a)] = \\ - r_a \cdot \nabla P_a + \nabla\left[r_a \cdot \mu_a \cdot \left(\nabla U_a + (\nabla U_a)^T\right)\right] + S_{Ma} + M_{a\beta}\end{aligned} \quad (3)$$

The interphase momentum exchange terms are equal and opposite, so the net forces sum to zero:

$$M_{a\beta} + M_{\beta a} = 0 \quad (4)$$

Since the volume fractions sum up to unity, an additional constraint is the volume conservation equation:

$$r_a + r_\beta = 1 \quad (5)$$

2.2 Turbulence modeling

The Shear Stress Transport (SST) turbulence model (Ref. [7]) has been applied for both air and oil. The SST model switches between the standard k-ε (for the flow away from the walls) and the k-ω turbulence model (for the vicinity of walls) using a blending function to model the near wall conditions. The influence of the air bubbles on the oil turbulence (bubble induced turbulence) has been taken into consideration by applying the Sato's enhanced eddy viscosity model (Ref. [8]). Furthermore, to account for the random (dispersive) influence of the turbulent eddies on the bubbles the concept of turbulent dispersion force has been applied. This force is proportional to the local bubble concentration (void fraction) gradient, i.e.

$$M^{TD}_{a\beta} = -M^{TD}_{\beta\alpha} = -C_{TD} \cdot \rho_a \cdot k_a \cdot \nabla r_a \quad (6)$$

This form of the turbulence dispersion force was first introduced in Ref. [9]. In the literature there are no general recommendations for the coefficient CTD. In this study it was set to 0.1.

2.3 Interphase momentum exchange terms

Due to the loss of information in the averaging process the interfacial momentum exchange term Maβ in Equation 3 needs to be closed in terms of known variables. A discussion on closed formulations of the various interphase momentum exchange terms for bubbly and slug flow can be found in Ref. [10] and [11].

The drag force $D\alpha,\beta$ as the most important interphase force resulting from the mean relative velocity between the two phases is included. The total drag per unit volume is:

$$D_{\alpha\beta} = \frac{3}{4}\cdot\frac{C_D}{r}\cdot r_\beta^*\cdot\rho_a\cdot\left|U_\beta - U_\alpha\right|\cdot\left(U_\beta - U_\alpha\right) \quad (7)$$

$$r_\beta^* = \begin{cases} \max\left(r_\beta, r_{\min}\right), & r_\beta < r_{\max} \\ \max\left(\dfrac{1-r_\beta}{1-r_{\max}}, r_{\min}\right), & r_\beta > r_{\max} \end{cases} \quad (8)$$

where r_β is the volume fraction of the dispersed phase and r_{min}, r_{max} are user specified coefficients.

In this work it is supposed that in the low volume fraction region the dispersed phase consists of single sized bubbles or droplets. Break-up as well as coalescence mechanisms are neglected. For the determination of the drag coefficient the generalised model found in Ref. [12] has been employed:

$$C_D = C_{D\infty}\cdot E'' \quad (9)$$

$$C_{D\infty} = \frac{4}{3}\cdot\frac{\rho_l - \rho_g}{\rho_l}\cdot g\cdot d\cdot\frac{1}{u_\infty^2} \quad (10)$$

$$u_\infty = \frac{u_{b1}\cdot u_{b2}}{\sqrt{{u_{b1}}^2 + {u_{b2}}^2}} \quad (11)$$

$$u_{b1} = \frac{1}{18}\cdot\frac{\rho_l - \rho_g}{\mu_l}\cdot g\cdot d^2\cdot\frac{3\cdot\mu_g + 3\cdot\mu_l}{3\cdot\mu_g + 2\cdot\mu_l} \quad (12)$$

$$u_{b2} = \sqrt{\frac{2\cdot\sigma}{d\cdot\left(\rho_l - \rho_g\right)} + \frac{g\cdot d}{2}} \quad (13)$$

$$E'' = \left(1-\alpha_g\right)\cdot\left[\left(1-\alpha_g\right)^m + \left(4.8\cdot\frac{\alpha_g}{1-\alpha_g}\right)^m\right]^{-\frac{2}{m}} \quad (14)$$

where m=0.25. In Figure 1 the relationship between the drag force coefficient and the dispersed phase volume fraction for an assumed bubble diameter d=0.005 m is illustrated.

Lift force Lα,β represents the transverse force due to rotational strain, velocity gradients, or the presence of walls. A general equation for the lift force is given by:

$$L_{\alpha\beta} = C_L\cdot r_\beta\cdot\rho_a\cdot\left(U_\beta - U_\alpha\right)\times\left(\nabla\times U_a + 2\cdot\Omega\right) \quad (15)$$

In literature, a wide range of values can be found for the lift force coefficient. For ideal laminar flow the value of 0.5 can be determined for the lift force coefficient C_L. In Ref. [13] the authors have performed experiments of single bubbles in simple shear flows and have found positive and negative values for the lift force coefficient, depending upon the bubble diameter. In this study the coefficient C_L has been determined with respect to Ref. [14]. In Figure 2 a plot of the C_L coefficient versus the bubble diameter is presented. The lift force is considered negligible for volume fractions greater than r_β>0.1 according to Ref. [15].

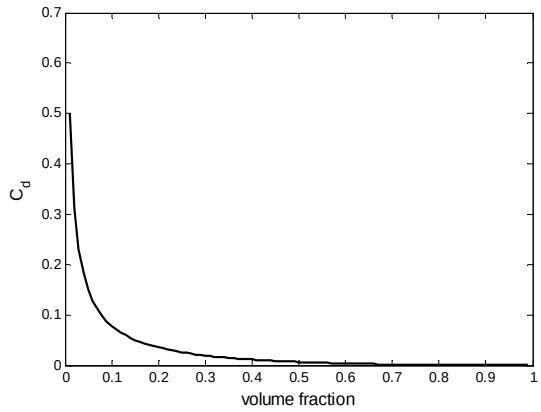

Fig. 1. Drag force coefficient versus volume fraction for assumed bubble diameter d=0.005m.

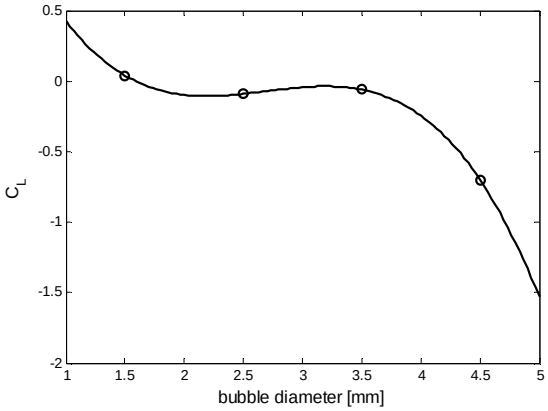

Fig. 2. Lift force coefficient versus bubble diameter size.

The virtual mass force D_{vm} is the last interphase momentum exchange term that has been considered. It is a transient force and can be understood by considering the change in kinetic energy of the continuous phase surrounding an accelerating dispersed phase. If the dispersed phase is accelerated relative to the continuous one, part of the surrounding continuous phase has to be accelerated as well. This additional force contribution is called the virtual mass force. Ref. [8] gives a general equation for this force. The virtual mass coefficient C_{VM} is dependent on the volume

fraction. A graph of this relationship is shown in Fig. 3.

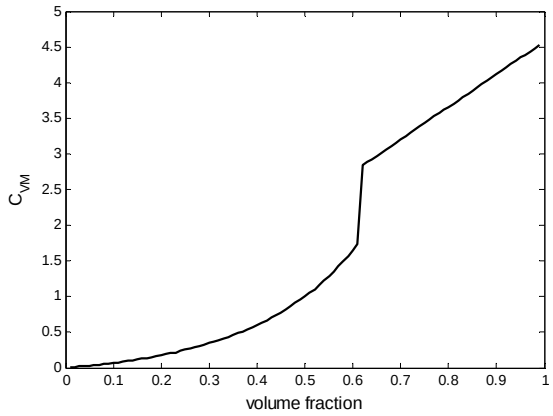

Fig. 3. Virtual mass force coefficient versus volume fraction.

3 Computational model

3.1 Geometry model

A three dimensional view of the geometry model of the test rig pipework is shown in Figure 4. It is a complex layout consisting basically of four pipe segments: a) One vertical section with the nominal flow in the direction of gravity. It has a length of about 0.5 *m*. b) Two horizontal sections with lengths 0.85 *m* and 1.25 *m* and finally c) One inclined section. The inclination of the last segment is about 60^o. The pipe segments are connected with bends of different radius. The bearing chamber is located at the top of the vertical pipe segment. The scavenge pump's inlet is located on the right side at the top of the inclined pipe segment. The mixture's nominal flow and gravity have the same direction at the vertical segment. At the inclined segment they have opposite directions.

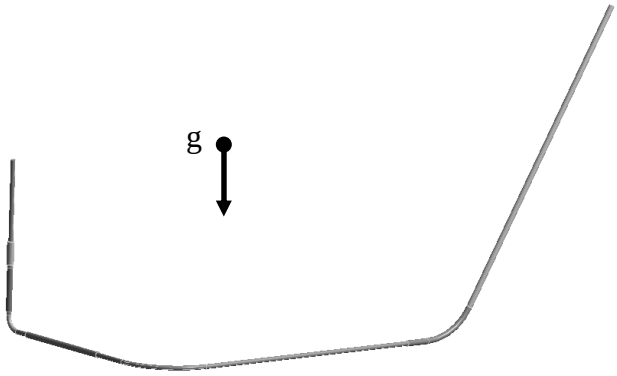

Fig. 4. Three dimensional view of the geometry model of the scavenge pipe

A schematic of the test rig, where the experiments took place, is illustrated in Fig. 5. As may be noticed, two high speed cameras (HSCs) have been installed at two positions of the test rig. The HSCs were utilized observing the developed oil-air phase flow pattern and how it changes with respect to time. The HSCs can capture up to 2000 frames per sec. Pictures showing the actual test rig at these two positions are given in Fig. 5. The inside wall area of the horizontal pipe section has been marked appropriately to make possible the measurement of the oil-air mixture velocity by visual means.

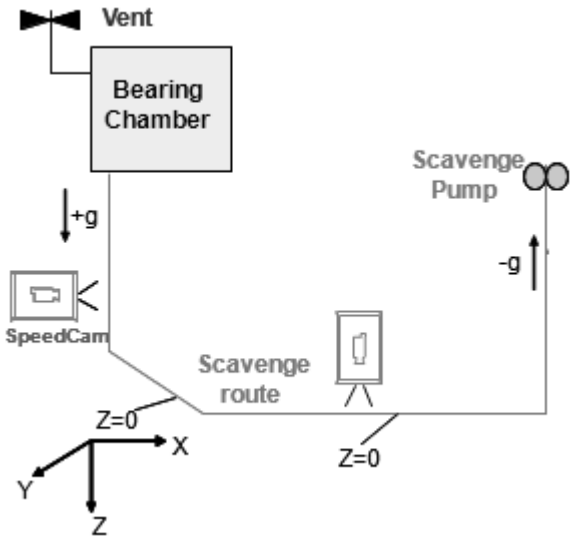

Fig. 5. Schematic of the experimental facility

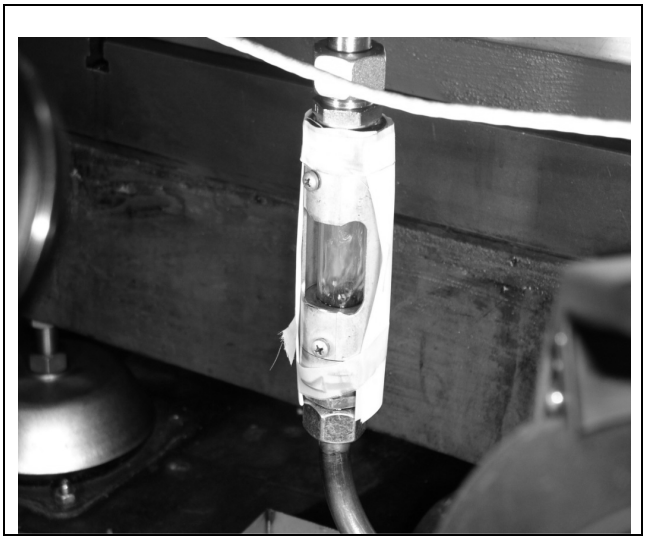

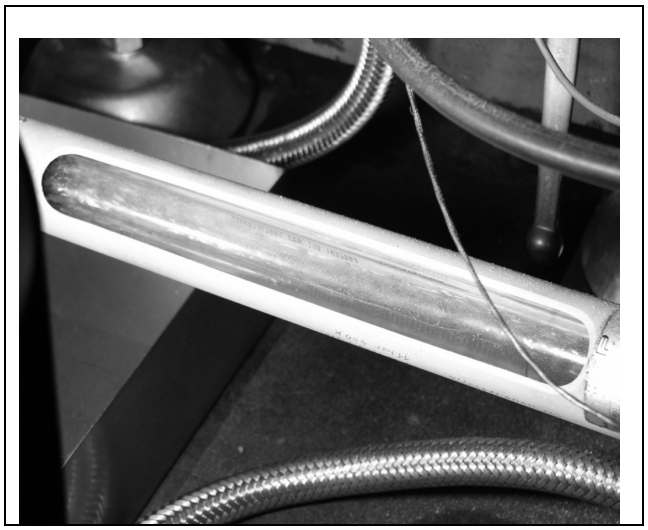

Fig. 6. Actual test rig. Vertical section on the upper part and horizontal section on the lower part of the figure

3.2 Grid generation

The geometry model has been meshed using ANSYS built-in mesh generator. An O-ring type mesh has been created. The reason for making this choice was the resulting good volume to area ratio of the generated elements. The mesh consisted mainly of hexahedral elements. A total number of 500320 elements and 631495 nodes have been used to discretize the problem. Detailed views of the mesh are shown in Figures 7 & 8.

Fig. 7. General view of the finite element mesh at the pipework's vertical section.

A mass flow rate of 0.00286 *kg/s* and 0.0396 *kg/s* has been considered for air and oil respectively at the pipe inlet. A medium intensity turbulence model has been set at the scavenge pipe's entrance. An average static pressure of 0.3 *bar* was set at the outlet. No-slip conditions were supposed for both oil and air at the pipe's walls.

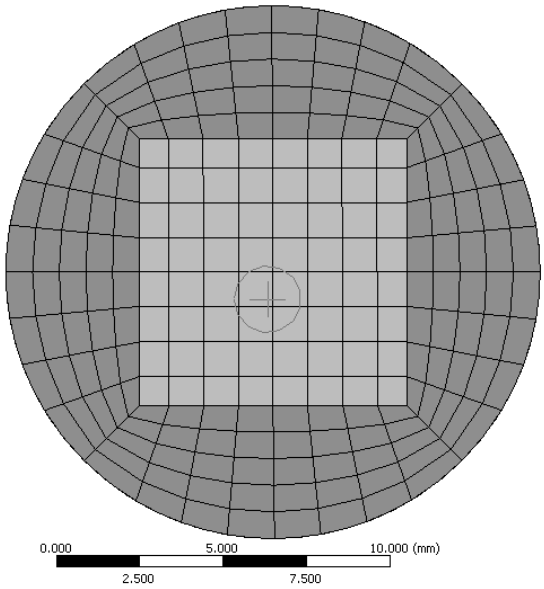

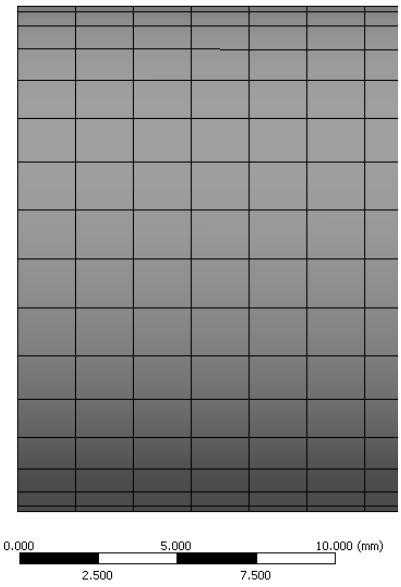

Fig. 8. Detail view of the finite element mesh at the scavenge pipe inlet (upper part: front view, lower part: side view). The circle has a diameter of 2 mm.

The numerical solution of the continuity and momentum equations has been obtained using the CFD code ANSYS CFX 11.0, which is a vertex-centered code based on the finite volume numerical method. The Navier-Stokes conservation equations described above are solved using an element-based finite volume method (Ref. [16]). The discretization of the conservation equations is time explicit. The conservation equations are integrated over each control volume, volume integrals are converted to surface integrals using Gauss' divergence theorem, and surface fluxes are evaluated in exactly the same

manner at the two control volumes adjacent to an integration point. The mass flows are discretized carefully following the interpolation scheme proposed by Ref. [17]. For the integration the First Order Backward Euler method and the Upwind advection scheme have been employed. The linear system of equations is solved using a coupled algebraic multigrid technique Ref. [18]. For investigation of flow solver convergence the gas holdup and the global mass balances for both phases were defined as monitored target variables.

3.3 Volume fraction correlations

For the implementation of the generalized interphase momentum exchange models a numerical model approximating the local volume fraction has been coded and implemented through the CCL option in ANSYS CFX 11. The implemented numerical model was taken from Ref. [19]. A 3D graph showing the dependence of the volume fraction from the liquid and gas velocities is shown in Fig. 9.

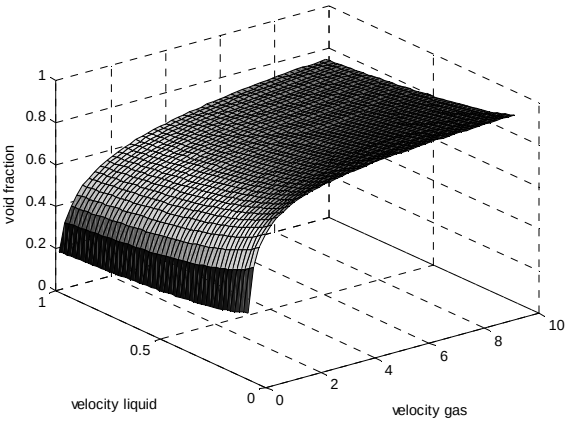

Fig. 9. 3D mesh graph of volume fraction & gas and liquid velocities

4 Numerical results

The picture sequence Fig. 10 - Fig. 12 shows the flow predicted by the CFD calculation. From the numerical results we understand that the flow at the lower part of the vertical segment is annular while at the horizontal and inclined part slug flow. In Fig. 13 a snapshot, from the videos taken with the HSCs, of the actual oil-air mixture flow in the horizontal pipe section is given. The flow at the right part of the segment is stratified. Due to gravity oil is concentrating at the lower part of the pipe's cross section. At the middle a wave of oil and air mixture that covers the whole pipe cross section area is present. At the left part a new wave of oil and air is just entering the pipe segment.

In greater detail, in Fig. 14 the flow in a cross section located at the lower part of the vertical segment is shown for two different time instants. As observed the oil film thickness at the pipe's wall changes with respect to time. In Fig.15 a snapshot presenting the actual oil-air mixture flow in the vertical segment is shown. The flow is annular because most of the oil is attached on the pipe's walls.

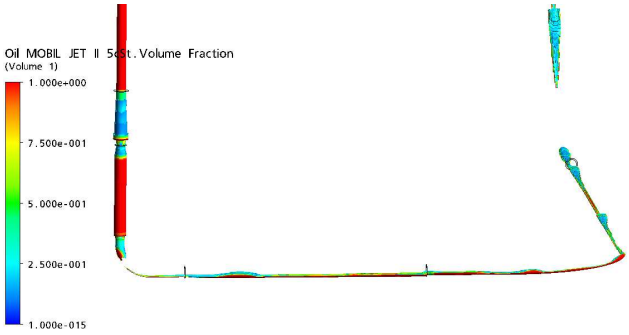

Fig. 10. Oil volume fraction distribution at time t=0.32 s (values below 0.1 are not shown)

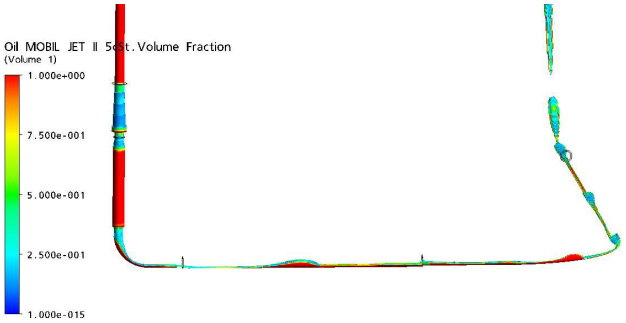

Fig. 11. Oil volume fraction distribution at time t=0.42 s (values below 0.1 are not shown)

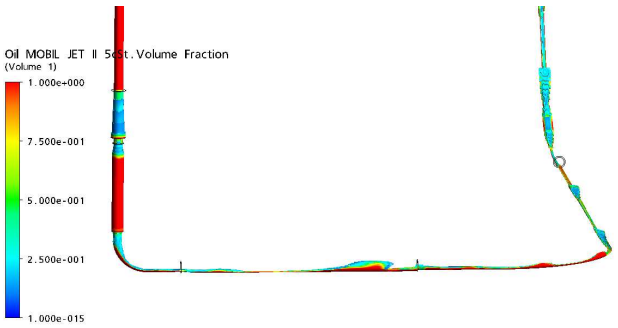

Fig. 12. Oil volume fraction distribution at time t=0.48 s (values below 0.1 are not shown)

CFD succeeds in predicting the different developed flow patterns at the different locations of the pipework. The computational results are in full agreement with the observations made with the high speed video camera.

Fig. 13. Snapshot of the oil air mixture flow in the horizontal pipe section

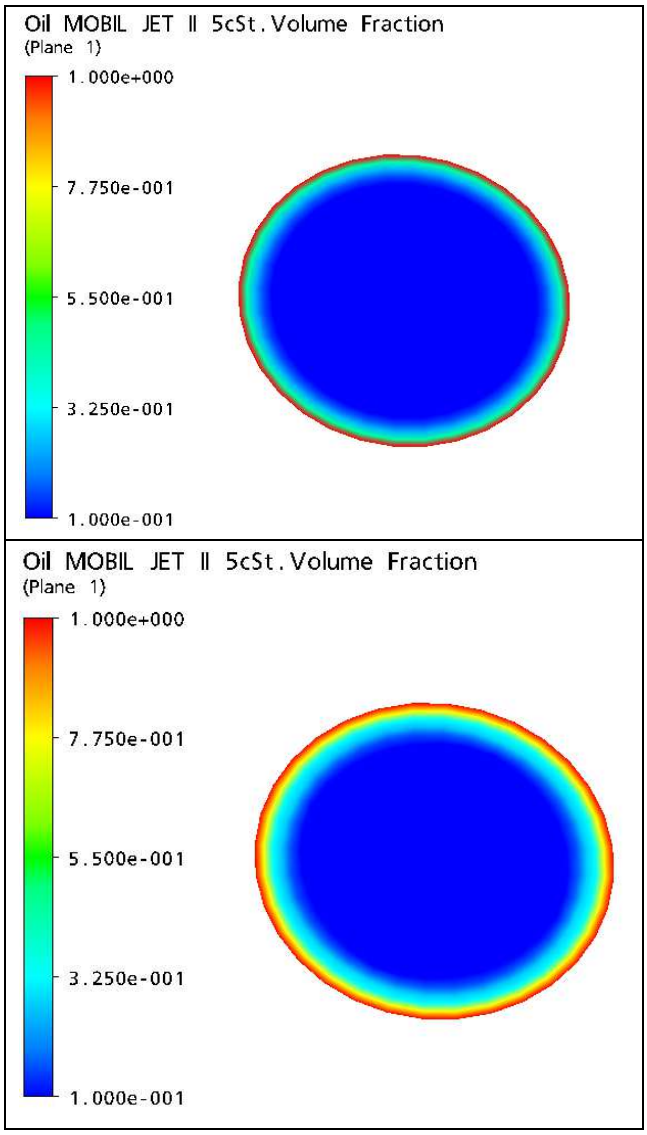

Fig. 14. Oil volume fraction distribution at time t=0.64 s (upper part) and t=0.86s (lower part)

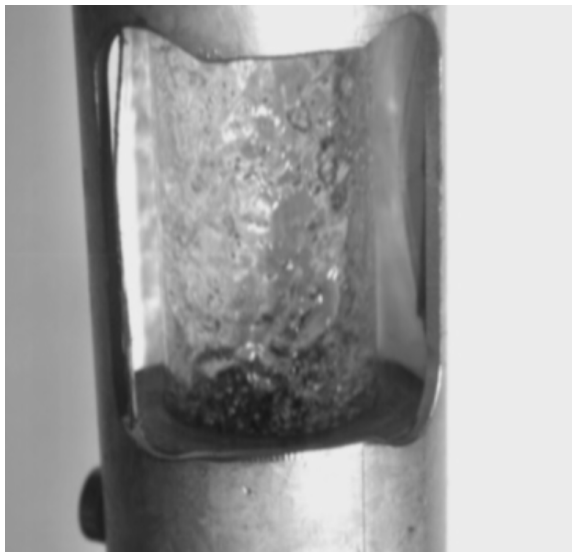

Fig. 15. Snapshot of the oil air mixture flow in the vertical pipe section

CFD calculations also succeeded in predicting the mixture flow at the contraction and expansion areas of the test rig pipework, e.g. see Fig. 16. At the left part of Fig. 16 the scavenge pipe diameter increases suddenly from 18 mm to 25 mm. At the right part of Fig. 16 the diameter reduces suddenly from 25 mm to 16 mm. In both cases the recirculation zones, the pressure drop and the reattachment length have been computed correctly by ANSYS CFX 11 (Ref. [21]).

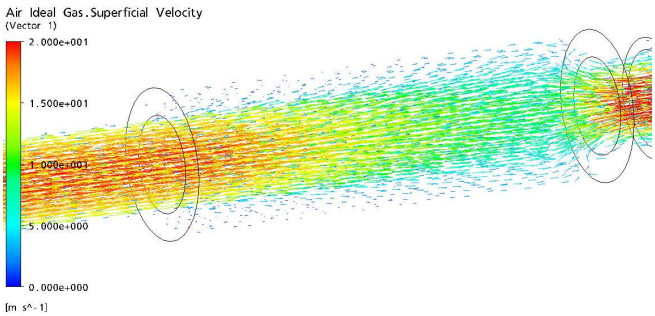

Fig. 16. Vector plot of air superficial velocity

Finally, CFD succeeded also in computing correctly the mechanism that generates the slug flow at the horizontal segment of the pipework. According to Ref. [20] slug flow is generated due to the continuously decelerating motion of the fluid. Wall friction is responsible for the fluid's deceleration. As an effect the fluid velocity is constantly being reduced and the area occupied by the fluid in the pipe's cross section increased. Air which has to pass now through a narrower passage

accelerates. As a result a wave of oil is created which eventually leads to generation of the slug flow. As can be observed in Fig. 17 the oil volume fraction is continuously increasing (from left to right) in the horizontal pipe segment. Fig. 18 shows that the oil velocity at the lower part of the horizontal pipe segment is being reduced. On the contrary, the upper part which is mainly occupied by air is accelerating.

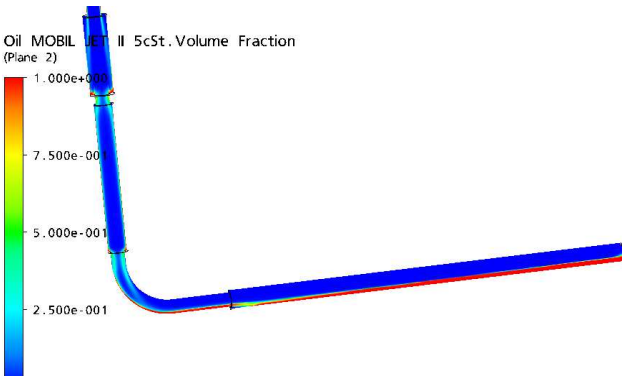

Fig. 17. Oil volume fraction at the horizontal segment of the pipework at t=0.1 s

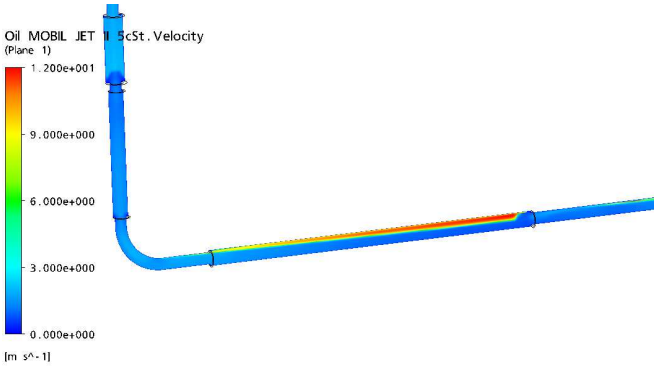

Fig. 18. Oil velocity at the horizontal segment of the pipework at t=0.1 s

5 Conclusion

A number of CFD calculations have been carried out to investigate whether CFD can predict the oil-air mixture flow within the scavenge pipe of a real aero engine. The commercial CFD package ANSYS CFX 11 has been utilized for the computations. High speed cameras have been installed at two different locations of the experimental test rig to verify the computational results. One was located at the vertical and the other one at the horizontal pipe segment. The formation and propagation of different flow patterns - wavy annular, stratified and slug flow – at different locations of the pipework were successfully predicted by the numerical model proposed by the authors. Perturbations acting on the boundary conditions and disturbances on the mixture flow caused by geometric irregularities were some of the factors identified to play an important role on the successful prediction of the different flow patterns. Computational results and experimental observations agreed well. However, a very detailed comparison was not possible due to the uncertainties of the flow conditions at the inlet and outlet (pressure distribution, mass flow distribution) and due to the uncertainties in the numerical model (bubble size diameter, e.t.c.).

It was again shown that the transition from segregated to slug flow is dependent from the wall friction and the action of gravity. Gravity is important both in the horizontal and inclined segments of the pipework. Especially, in the inclined part it is observed that the shear forces between air and oil were not capable of overcoming the opposing gravity force. Small waves of oil and air merged into larger slugs that were eventually driven outside the pipework by pressure forces. CFD was also successful in predicting the recirculation zones located at different parts of the pipework and in particular at pipework diameter transitions.

Detailed experimental investigations are necessary for acquiring reliable data that will be used for the further development and improvement of the existing numerical models.

References:

[1] Th. Frank, P.J. Zwart, E. Krepper, H.-M. Prasser and D. Lucas, Validation of CFD models for mono- and polydisperse air-water two-phase flows in pipes, Nuclear Engineering and Design 238 (2008) 647-659.

[2] K. Ekambara, R.S. Sanders, K. Nandakumar and J.H. Masliyah, CFD simulation of bubbly two-phase flow in horizontal pipes, Chemical Engineering Journal 144 (2008) 277-288.

[3] C. Vallee, T. Hohne, H.-M. Prasser and T. Suhnel, Experimental investigation and CFD simulation of horizontal stratified two-phase flow phenomena, Nuclear Engineering and Design 238 (2008) 637-646.

[4] T. Hoehne, Experiments and numerical simulations of horizontal two phase flow regimes, Seventh International Conference on CFD in the Minerals and Process Industries, CSIRO, Melbourne, Australia, 9-11 December 2009.

[5] S. Kanarachos and M. Flouros, The impact of flow inlet conditions on the two phase flow pattern and the heat transfer in a scavenge pipe of an Aero engine bearing chamber sealed with brush seals, 5th International Gas Turbine

Conference, Brussels, Belgium, 27-28 October 2010.
[6] I. Kataoka and A. Serizawa, Basic equations of turbulence in gas-liquid two phase flow, Int. J. Multiphase Flow 15 (1989) 843-852
[7] F. Menter, Two-equation eddy-viscosity turbulence models for engineering applications, AIAA J, 32 (1994) 1598-1605.
[8] M. Ishii and T. Hibiki, Thermo-Fluid Dynamics of Two Phase Flow, Springer, 2010
[9] M. Lopez de Bertodano, Turbulent Bubbly Flow in a Triangular Duct, Ph. D. Thesis, Rensselaer Polytechnic Institute, Troy New York, 1991.
[10] C. R. Maliska, A. F. C. da Silva, R. V.P. Rezende and I. C. Georg, Interphase Forces Calculation for Multiphase Flows, 1º Encontro Brasileiro sobre Ebulição, Condensação e Escoamento Multifásico Líquido-Gás, Florianópolis, 28-29 April 2008
[11] T. Frank, Numerical Simulation of Slug Flow Regime for an Air-Water Two Phase Flow in Horizontal Piopes, The 11th International Topical Meeting on Nuclear Reactor Thermal-Hydraulics. Avignon, France, 2-6 October 2005.
[12] M. Simonnet, C. Gentric, and E. Olmos, Experimental determination of the drag coefficient in a swarm of bubbles, Chem. Eng. Sci. 62 (2007) 858-866.
[13] A. Tomiyama, H. Tamai, I. Zun and S. Hosokawa, Transverse migration of single bubbles in simple shear flows, Chemical Engineering Science 57 (2002) 1849-1858.
[14] B. Ford and E. Loth, Forces on ellipsoidal bubbles in a turbulent shear layer, Phys. Fluids, 10 (1998) 178-188.
[15] S. W. Beyerlein, R. K. Cossmann, and H. Richter, Prediction of bubble concentration profiles in vertical turbulent two-phase flow, Int. J. Multiphase Flow 11 (1985) 629-641.
[16] M.J.Raw, A coupled algebraic multigrid method for the 3D Navier-Stokes equations, Proceedings of the 10th GAMM Seminar, 1994.
[17] C.M. Rhie and W.L. Chow, A numerical study of the turbulent flow past an isolated airfoil with trailing edge separation, AIAA Journal 11 (1982) pp.1525-1532
[18] M.J. Raw, Robustness of coupled algebraic multigrid for the Navier-Stokes equations, Proceedings of the 34th Aerospace and Sciences Meeting & Exhibit, AIAA 96-0297, 1996.
[19] A.J. Ghazar and C.C. Tsang, Void fraction and flow patterns of two phase gas-liquid flow in various pipe inclinations, Proceedings of the 7th International Conference on Heat Transfer, Fluid Mechanics and Thermodynamics, Turkey, 19-21 July 2010.
[20] T. Frank, Numerical simulation of slug flow regime for an air-water two phase flow in horizontal pipes, Proceedings of the 11th International Topical Meeting on Nuclear Reactor Thermal-Hydraulics, France, 2-6 October 2005.
[21] V.G. Kourakos, P. Rambaud, S. Chabane, D. Pierrat, and J.M. Buchlin, Two-phase flow modeling within expansion and contraction singularities, Computational Methods in Multiphase Flow V, WIT Press, 2009.

Nomenclature

d	bubble diameter
D	drag per unit volume
	dispersion coefficient
CD	drag force coefficient
CL	lift force coefficient
C_{vm}	virtual mass force coefficient
C_{TD}	turbulent dispersion coefficient
M	interfacial momentum exchange term
P	pressure
r	phase volume fraction
t	time
u	liquid velocity
U	average velocity
ρ	Reynolds averaged density
μ	dynamic viscosity
Γ	mass flow rate per unit volume
S	external sources
E_0	Eotvos number
k_a	turbulent kinetic energy of the continuous phase
μ	dynamic viscosity
σ	surface tension

subscripts

a	continuous phase
β	dispersed phase
l	liquid
g	gas

superscripts

TD	turbulent dispersion